

Reaching the Excitonic Limit in 2D Janus Monolayers by In Situ Deterministic Growth


Ying Qin, Mohammed Sayyad, Alejandro R.-P. Montblanch, Matthew S. G. Feuer, Dibyendu Dey, Mark Blei, Renee Sailus, Dhiren M. Kara, Yuxia Shen, Shize Yang, Antia S. Botana, Mete Atature,* and Sefaattin Tongay*

Named after the two-faced Roman god of transitions, transition metal dichalcogenide (TMD) Janus monolayers have two different chalcogen surfaces, inherently breaking the out-of-plane mirror symmetry. The broken mirror symmetry and the resulting potential gradient lead to the emergence of quantum properties such as the Rashba effect and the formation of dipolar excitons. Experimental access to these quantum properties, however, hinges on the ability to produce high-quality 2D Janus monolayers. Here, these results introduce a holistic 2D Janus synthesis technique that allows real-time monitoring of the growth process. This prototype chamber integrates in situ spectroscopy, offering fundamental insights into the structural evolution and growth kinetics, that allow the evaluation and optimization of the quality of Janus monolayers. The versatility of this method is demonstrated by synthesizing and monitoring the conversion of SWSe, SNbSe, and SMOSe Janus monolayers. Deterministic conversion and real-time data collection further aid in conversion of exfoliated TMDs to Janus monolayers and unparalleled exciton linewidth values are reached, compared to the current best standard. The results offer an insight into the process kinetics and aid in the development of new Janus monolayers with high optical quality, which is much needed to access their exotic properties.

Y. Qin, M. Sayyad, M. Blei, R. Sailus, Y. Shen, S. Yang, S. Tongay
Materials Science and Engineering
School for Engineering of Matter
Transport and Energy
Arizona State University
Tempe AZ 85287, USA
E-mail: sefaattin.tongay@asu.edu

A. R.-P. Montblanch, M. S. G. Feuer, D. M. Kara, M. Atature
Cavendish Laboratory
University of Cambridge
J. J. Thomson Avenue, Cambridge CB3 0HE, UK
E-mail: ma424@cam.ac.uk

D. Dey, A. S. Botana
Department of Physics
Arizona State University
Tempe AZ 85287, USA

 The ORCID identification number(s) for the author(s) of this article can be found under <https://doi.org/10.1002/adma.202106222>.

© 2021 The Authors. Advanced Materials published by Wiley-VCH GmbH. This is an open access article under the terms of the Creative Commons Attribution License, which permits use, distribution and reproduction in any medium, provided the original work is properly cited.

DOI: 10.1002/adma.202106222

1. Introduction

To date, 2D transition metal dichalcogenides (TMDs) have shown great promise with their unique excitonic, superconducting, as well as topological properties toward applications in quantum information, optoelectronics, and photonics fields.^[1,2] These 2D TMDs are essentially made of metal cations that are sandwiched between the same type of chalcogen atoms such as Se–W–Se for WSe₂. A sister material system, Janus monolayer, is created by replacing the chalcogen anion layer with another dissimilar chalcogen layer to form S–W–Se or SWSe.^[3] In this unique atomic arrangement, Janus monolayers lack both the inversion and mirror symmetry, contain vertical colossal polarization field, and offer a completely new set of properties that are superior to their classical counterparts.^[3–6]

Breaking the mirror symmetry within a unit-cell-thick material, however, comes with immense challenges. Foremost, 2D miscible anionic alloys such as MoS₂Se and WS₂Se contain S and Se atoms that are randomly distributed on either side of the transition metal surface without any symmetry.^[7,8] Thus, 2D alloys are thermodynamically preferred over their 2D Janus SMOSe or SWSe counterparts, where S and Se atoms are separated from each other on either side of the (top or bottom) surfaces. In their synthesis, the goal is to prevent TMDs from alloying, placing atoms in their prescribed positions to realize a two-faced Janus geometry while simultaneously achieving a high crystal quality.

Recognizing these opportunities and challenges, previous work from our team and others has employed high-temperature processing, epitaxial conversion, and pulsed laser deposition to transform 2D classical layers into Janus structures.^[4,5,9–12] These growth methods are at their primal stages and produce low-quality monolayers; first, these techniques require intense growth conditions, and thus Janus monolayers are at the cusp of alloying or heavily defected with poor electronic/optical quality.^[4,5,9,10] Thus, the photoluminescence (PL) of SMOSe and SWSe Janus monolayers exhibits a large bound exciton peak related to defects or a rather broad PL peak due to strain, alloying, and defects. Second, these techniques lack in situ growth monitoring tools and, therefore, Janus monolayers

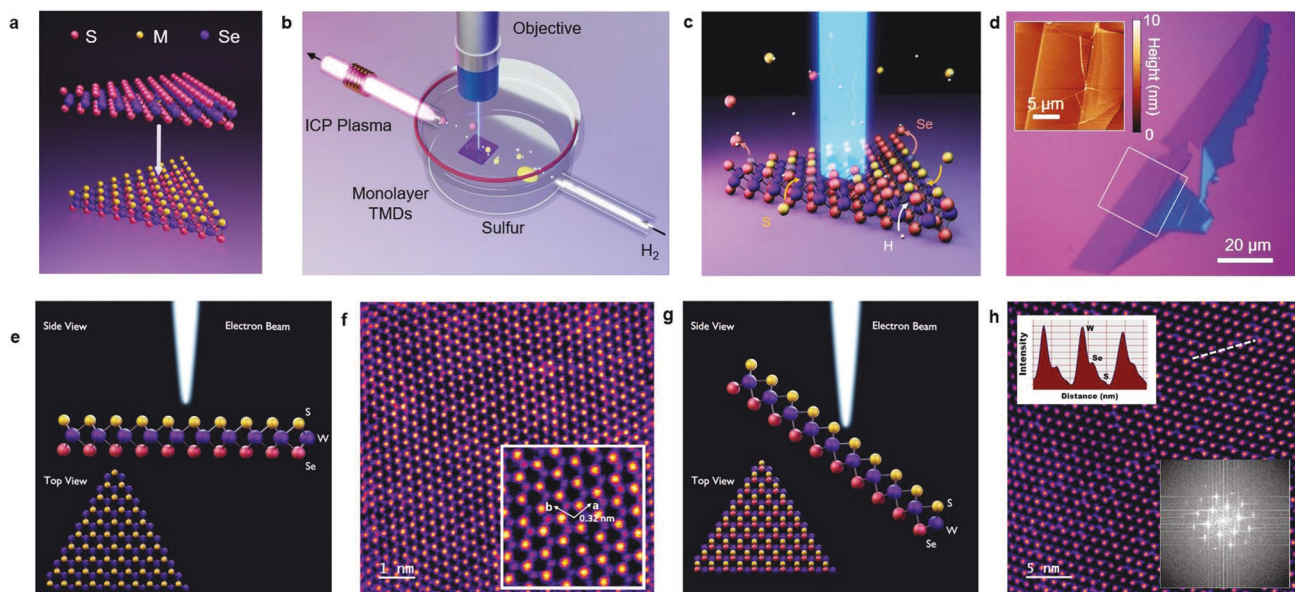


Figure 1. a) Schematic representation of the structural evolution from TMD monolayer to Janus after the SEAR process. b) Schematic diagram of our custom-designed plasma chamber enabling in situ optical measurement of the SEAR process. ICP labels the inductively coupled plasma ignited at the downstream of chamber setup. c) Schematic diagram of the in situ Raman measurement process. d) Optical image of exfoliated WSe₂ monolayer on a SiO₂/Si substrate. Inset: atomic force microscopy (AFM) height profile measured in the framed area. e, g) Schematic representation of planar versus tilted view of the monolayer under the electron optics column. f) False-color MAADF-STEM microscopy image of monolayer SWSe at 0° tilt angle. Inset: zoom-in showing the calculated lattice constant $a = b = 3.2 \text{ \AA}$. h) MAADF-STEM microscopy image of monolayer SWSe at 20° tilt angle. Insets: corresponding fast-Fourier transform (FFT) and line profile showing diminishing intensity of atoms due to Z-contrast imaging.

are only produced on a trial-and-error basis. The process is low yield in that only a fraction (<0.1%) of the entire sample transforms into Janus monolayers. Thus, the use of large-area chemical vapor deposition (CVD) monolayers is essential to access a small segment of Janus monolayers. Third, limiting the process to handle CVD-grown classical monolayers prevents reaching the electronic/optical (excitonic) quality needed for probing theoretically predicted exotic quantum properties in Janus monolayers^[13–15] due to the high starting defect density in CVD monolayers.^[16,17] Lastly, without the in situ growth monitoring tools, the growth dynamics of 2D Janus monolayers remains unknown. This ultimately prevents the field from expanding the library of 2D Janus monolayers.

Here, we introduce an ambient-temperature 2D Janus monolayer synthesis technique that integrates in situ optical spectroscopy to monitor and optimize the growth to achieve quantum-quality Janus materials, with extremely narrow exciton linewidths and fewer defects, by converting them from their parent classical layers (Figure 1a). The microresolution deterministic approach can handle CVD or exfoliated monolayers, with a wide range of TMDs, to experimentally realize a variety of Janus structures. The overall reaction is carried out inside a homemade glass chamber (Figure 1b) with a large-diameter optical window. The chamber is coupled to Raman and PL spectrometers for real-time data collection to assess how the reaction proceeds and is supported by a three-axis micromanipulator stage for precise measurement on the desired monolayers. The prototype chamber was designed after a careful consideration of the flow dynamics and yield of the neutral radicals in the hydrogen plasma, as well as the thickness of the top glass piece that was also engineered to be compatible with the numerical aperture of the objective lens, thus

improving the spectroscopic signal received from monolayer samples (for more details, see the Experimental Section). N6.0 ultrapure hydrogen gas is introduced through the upstream gas port, and the plasma is generated downstream using an inductively coupled radio-frequency (RF) generator (Figure 1b).

The typical process starts with selenium-based exfoliated or CVD-grown large-area monolayers, such as MoSe₂, WSe₂, or NbSe₂ (Figure 1d). Subsequently, the top surface is converted to sulfur using the selective epitaxial atomic replacement (SEAR) method to yield the monolayer Janus TMD counterpart.^[9] Here, the pressure within the chamber is tuned to a few hundred mTorr, such that the mean free path of the radicals is sufficiently high to favor etching of only the top chalcogen layer. Furthermore, the energy of the hydrogen and sulfur radicals is carefully tuned by modulating the power of the RF generator above the energy of the transition metal–selenium bond to remove Se atoms, but below the energy of the transition metal–sulfur bond to keep the sulfur surface intact (Table 1) after selenium vacancies (V_{Se}) are modified with reactive sulfur radicals (Figure 1c). Furthermore, when the top chalcogen layer is removed, the bond energy of the metal and the lower chalcogen layer increases, thus forbidding further stripping of lower chalcogen atoms. It should be noted that while with the increase in

Table 1. Calculated energy exchange for creating chalcogen vacancies and replacing chalcogen sites in a WX₂ monolayer.

Material Matrix	Process	Energy [eV]
WSe ₂	Se–V	0.183
WS ₂	S–V	0.193
WSe ₂	Se–S	–0.026

the plasma radical energy, processes with high formation energies can also occur, the quality of the end product is severely degraded, as the higher plasma radical energy is needed to create and replace sulfur atoms that will also result in creation of defects and vacancy formation.

High-resolution scanning transmission electron microscopy (HR-STEM) is performed to reveal the structure of the exfoliated Janus monolayer SWSe. Figure 1e,g shows the experimental setup under the electron optics column used to confirm the broken mirror symmetry structure of the Janus monolayers. The medium-angle annular dark-field (MAADF) STEM image in Figure 1f shows highly crystalline ($\approx 10^{10}$ defects cm^{-2}) Janus monolayer with an experimentally observed lattice constant of 3.2 Å (Figure 1f, inset), which is in excellent agreement with the values reported in the literature.^[6,18] The sample is further tilted at an angle of 20° (Figure 1g) to access the bottom selenium and top sulfur atoms simultaneously. Figure 1h shows the plan view MAADF-STEM microscopy image of the tilted Janus SWSe monolayer in the electron optical column. The top-left inset is the intensity of MAADF-STEM image along the dashed line and the bottom-right inset is the fast-Fourier transform (FFT). The annular dark field signal intensity diminishes more for the lighter elements along the line profile because of Rutherford scattering from the smaller nucleus of sulfur atoms. By collecting the intensity along the dashed line in Figure 1h, we clearly reveal the Janus structure with the intensity distribution (Figure 1h, top inset).

Figure 2a–c shows the collected Raman spectra from exfoliated TMD monolayers (MoSe_2 , WSe_2 , and NbSe_2), before (green) and after (red) the SEAR process. The respective TMD monolayers are fully converted into 2D Janus monolayers (red). The Raman spectra exhibit full-width at half-maximum (FWHM) as low as 3.8 cm^{-1} , which is close to our starting material with $\text{FWHM} \approx 3 \text{ cm}^{-1}$, highlighting the quality of the produced Janus monolayers.^[4,5] The measured Raman spectra match well with our corresponding theoretical phonon dispersion relations (shown on top of the Raman spectra) as well as with published

theoretical datasets.^[4,5,19,20] This demonstrates the efficacy of the deterministic Janus conversion process on exfoliated monolayers and even allows us to extend the library of 2D Janus monolayers by converting NbSe_2 monolayers for the first time to SNbSe Janus monolayers as demonstrated in Figure 2c.

2. In Situ Monitoring During Janus Conversion

Our time-resolved in situ Raman spectroscopy measurements on exfoliated WSe_2 sheets show the efficacy of the growth approach (Figure 3a,b) and offer insights into the Janus' conversion process. At first sight, time-resolved Raman spectra show that 2D classical TMD monolayers are not allowed, but instead the Janus structure forms from 2D classical sheets and eventually the structural conversion is completed. We selected different Raman spectra collected at different times (t_1 through t_4) as highlighted in Figure 3b,c. The Raman spectrum at t_1 corresponds to the exfoliated WSe_2 monolayers without any sign of Janus monolayer formation (Figure 3c, red). As the reaction proceeds, these classical 2D TMD monolayers slowly develop SWSe Janus peaks at t_2 , which increase in intensity as shown in t_3 (Figure 3c, blue and yellow). At t_2 and t_3 points, the Janus conversion is only partial, and full conversion is attained after t_4 (Figure 3c, green).

To quantitatively analyze the reaction kinetics, the most prominent Raman peaks of WSe_2 (A_1' at 250 cm^{-1}) and Janus SWSe (A_1 at 284 cm^{-1}) are fitted to a single Lorentzian, and the evolution of the peak position, its intensity, and FWHM are shown in Figure 3d. In the first 5 min, there is no visible change in the Raman spectra, which is likely related to the time required to build sufficient radical concentration and introduce V_{Se} defects to catalyze the conversion process. Eventually (shaded region in Figure 3d), the A_1' mode of exfoliated WSe_2 significantly stiffens from 250 to 261 cm^{-1} due to an increased number of V_{Se} vacancies and the resulting lattice contraction

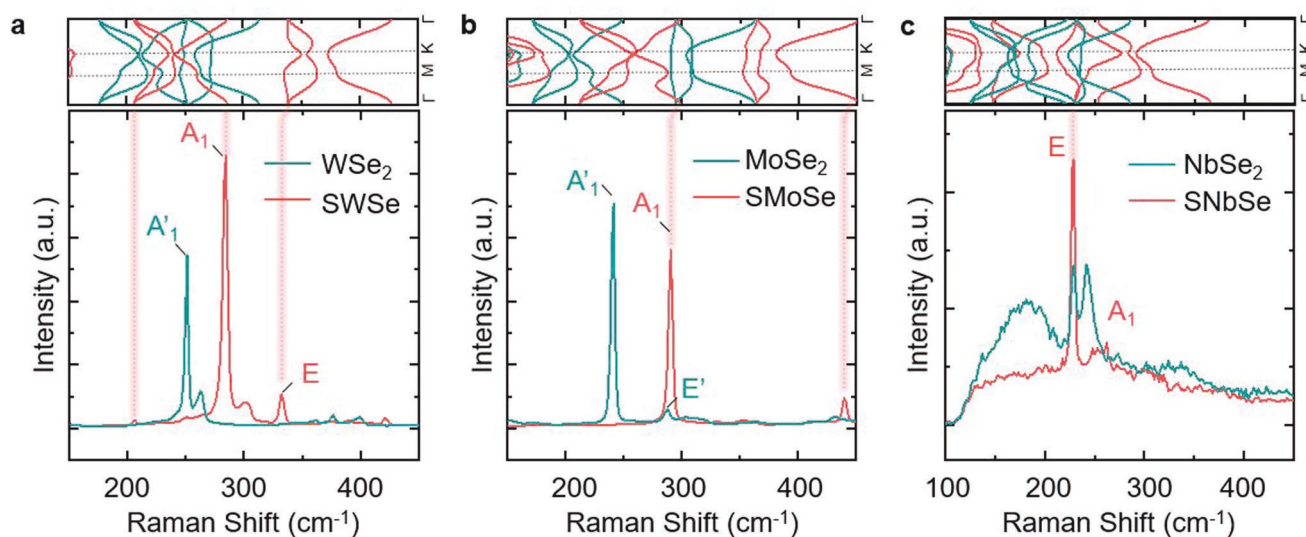


Figure 2. a–c) Raman spectra comparison of classical TMD monolayers with their Janus counterparts for classical WSe_2 and Janus SWSe (a), classical MoSe_2 and Janus SMoSe (b), and classical NbSe_2 and Janus SNbSe (c). The top panels show the corresponding calculated phonon dispersions for classical (blue) and Janus (red) monolayers. Note that (c) demonstrates the first Janus SNbSe monolayer realization.

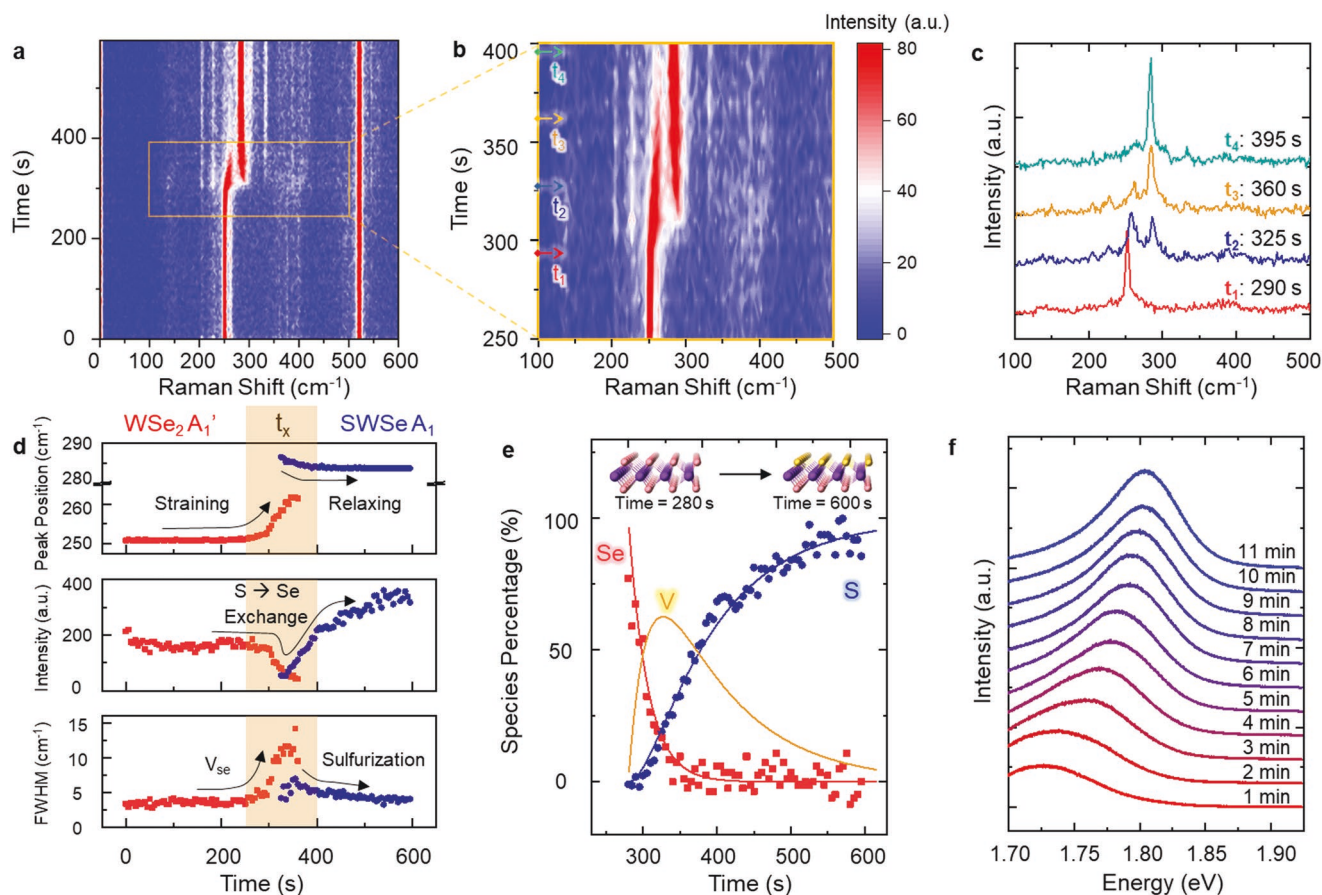


Figure 3. a) The first real-time insight into conversion from 2D classical to Janus monolayers through time-dependent Raman spectroscopy measurements. b) Zoom-in plots offering an insight into the conversion from classical WSe₂ to Janus structure. c) Raman spectra collected at given time spots, namely t_1 to t_4 . d) Time-resolved Raman peak position (top), intensity (middle), and FWHM (bottom). e) Top chalcogen coverage as a function of time. Scatter: percentages of S and Se on the top surface of monolayer estimated from corresponding Raman intensity. Line: simulated percentage evolution of S, Se, and vacancies as a function of processing time. f) Time evolution of PL spectrum during the Janus conversion process.

(top panel of Figure 3d). Increased V_{Se} density is also manifested through the reduction of A_1' peak intensity (middle of Figure 3d) and much-broadened peak features shown by FWHM values (bottom of Figure 3d).

Once the Janus peaks appear (see the t_x mark in Figure 3d), it is initially in its strained state with a peak position at 286.5 cm⁻¹, and it eventually relaxes into its established Raman frequency at 284 cm⁻¹ as the Janus conversion is completed by curing V_{Se} into sulfur-terminated sites. The peak intensity increases quickly after emergence, and the FWHM starts at a high value and slowly decreases. The behavior of both Raman peaks suggests that during the process, there is an intermediate state where the defect density is very high and the in situ process enables us to halt the Janus growth when Raman intensity, peak position, and FWHM are ideal for characterization/application. In addition to structural insights through time-dependent Raman measurements, in situ PL measurements allow one to monitor the PL FWHM and emission intensity as a function of the reaction coordinate. As shown in Figure 3f, the PL peak gradually blueshifts as the Se sites are gradually replaced by sulfur, from pure WSe₂ monolayer at ≈1.60 eV, to that of Janus SWSe at ≈1.80 eV.

Next, we offer more detailed estimates on the reaction kinetics under the assumption that the Raman peak is linearly proportional to the number of corresponding bonds, which is valid especially for 2D materials.^[17,21–23] This enables a correlation of Raman signals to estimate the density of Se/S sites through $\text{chalcogen\%} = (I_t - I_{\min}) / (I_{\max} - I_{\min})$, where I_{\max} and I_{\min} represent Raman peak intensity at any given time t , at the start, and end of the etching, respectively, for WSe₂, and vice versa, for SWSe peak. Since the reactive H radical concentration is orders of magnitude larger than the density of Se on the WSe₂ surface, we assume the concentration of H radicals stays constant throughout the process. Thus, the rate of Se etching (removal) can be estimated as $d\text{Se}(t)/dt \approx -\text{Se}(t)$, i.e., proportional to the number of Se sites left on the top surface (see the red plot in Figure 3e). Following a similar argument and assuming that sulfur removal from the top surface is negligible (since the radical energies are designed to be lower than the energy required to break W–S bonds), while considering that the total number of Se, S, and chalcogen vacancies add up to the total number of possible chalcogen sites, the time response of sulfur species on the top surface can be written as $d\text{S}(t)/dt \approx V(t) = \text{Se}(t=0) - \text{Se}(t) - \text{Se}(t)$, which is plotted as

the blue curve in Figure 3e. From the relationship of $Se(t, \%) + S(t, \%) + V(t, \%) = 100\%$, the concentration of vacancies can be calculated with respect to the processing time as shown in the yellow fitting in Figure 3e. We note that the time of 280 s after igniting plasma is marked as the start of the analysis for better data representation. The vacancy-rich time region from 280 to 400 s from the simulation matches very well with the qualitative analysis of the Raman trend from Figure 3d (see details of the analysis in the Supplementary Information).

3. Accessing Excitonic-Grade Properties in Janus Systems

Here, it is noteworthy to mention that the true advantage of our in situ growth technique lies in the ability to handle exfoliated monolayers, which are known to have higher crystalline, electronic, and optical quality compared to CVD-grown layers.^[16,24] Our results in Figure 4 present the comparison between Janus

monolayers produced from CVD grown (referred to as 2D CVD Janus) and exfoliated (referred to as 2D exfoliated Janus) classical 2D WSe₂ and MoSe₂ layers.

Raman spectra collected from Janus SWSe, WSe₂, SMOSe, and MoSe₂ from CVD and exfoliation methods exhibit similar characteristics, as shown in Figure 4a,b, and roughly similar FWHM profiles as discussed in Figure 4c. In contrast to Raman, PL spectra collected from classical, and Janus TMDs offer more insights into the quality of the monolayers since radiative excitonic, and nonradiative recombination channels are strongly influenced by the density and the nature of point defects/imperfections within the crystal structure.

Taking classical 2D WSe₂ and 2D Janus SWSe as an example (Figure 4d), the exfoliated WSe₂ monolayers show a much stronger and narrower PL peak compared to those from CVD-grown sheets. This is in accord with the literature, and the effect is simply attributed to the presence of vacancy defects and in-plane thermal stress at the substrate/2D layer interface.^[25,26] Much like classical 2D monolayers, 2D Janus monolayers

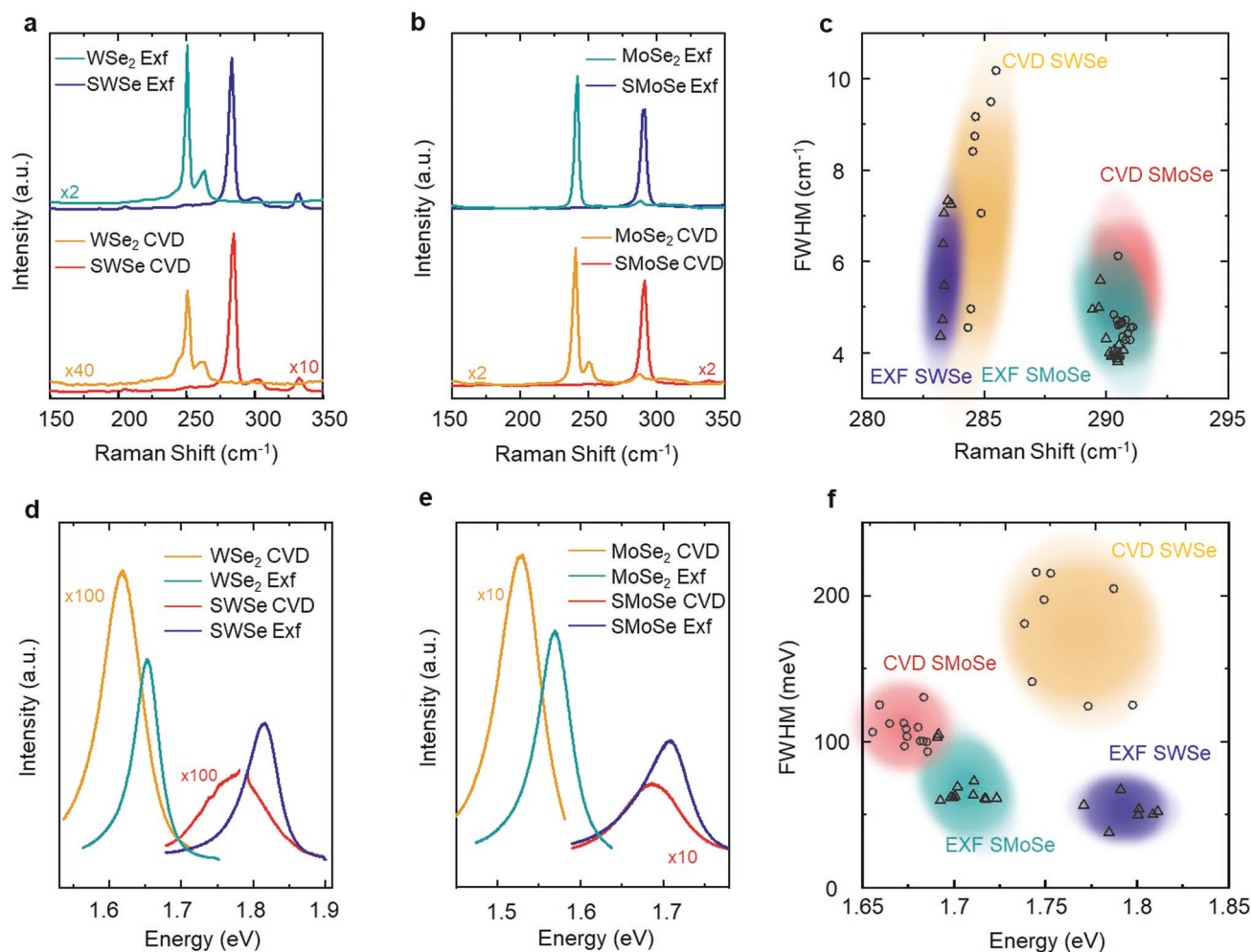


Figure 4. a,b) Comparison of representative Raman spectra collected on WSe₂ and MoSe₂ monolayer from exfoliation and CVD and the respective Janus structures. c) Statistical distribution of Raman position and FWHM of SMOSe and SWSe converted from CVD and exfoliated TMD monolayers. The shaded areas are guide to eye. d,e) Comparison of representative PL spectra collected on WSe₂ and MoSe₂ monolayers from exfoliation and CVD and the respective Janus structures. f) Statistical distribution of PL peak width and position of SMOSe and SWSe converted from CVD and exfoliated TMD monolayers.

created from exfoliated sheets exhibit a much stronger PL signal, and their FWHM values are improved on average by two times becoming as narrow as 38 meV for SWSe (Figure 4d) and 58 meV for SMOSe (Figure 4e). The discontinuity in the PL spectra observed in Janus SWSe from CVD is attributed to the Cr^+ impurity ions present in the sapphire substrate on which the parent TMD was grown.^[27] A series of studies on different samples also show that the PL FWHM improves by switching from CVD-grown classical layers to exfoliated ones (Figure 4f). A closer look at the PL analysis in Figure 4f shows that FWHM values of Janus monolayers produced from CVD-grown samples show a much greater degree (>50%) of variation in their values while those created from exfoliated ones have a greatly reduced variation and narrower FWHM profiles.

Figure 5 highlights the advantages of 2D Janus monolayers formed from exfoliated 2D sheets for cryogenic exciton spectroscopy. Figure 5a shows the PL spectra of CVD and exfoliated Janus SWSe at temperatures of 300 K (dark green spectrum for CVD and light-red spectrum for exfoliated) and 4 K (light green spectrum for CVD and dark red spectrum for exfoliated). Both the CVD and exfoliated monolayers were converted at the same time in the same chamber. While the CVD layer at 300 K has a PL peak of FWHM of 85 meV centered at 1.74 eV,

upon cooling down to 4 K, the PL spectrum is dominated by a broad signal (indicated by a blue arrow in Figure 5a) of an FWHM of 210 meV and centered at lower energy, 1.5 eV. This broad PL signature has traditionally been assigned in TMD monolayers to a defect-bound exciton PL band, X_B .^[28–30] The intensity of the peak at 1.82 eV (indicated by an orange arrow in Figure 5a), which is potentially of unbound excitonic nature, is in, this case, ten times lower compared to X_B .^[10,20] This behavior suggests that 2D CVD Janus monolayers have a large defect concentration and thus they lack sufficient quality to reliably perform low-temperature unbound-exciton spectroscopy measurements. In contrast, exfoliated Janus SWSe monolayers, which already at 300 K exhibit a narrower FWHM of 54 meV (light red spectrum in Figure 5a) as compared to CVD Janus monolayers (FWHM of 85 meV), show a cleaner spectrum when cooled down to 4 K (dark red spectrum in Figure 5a) with no X_B band and narrower lines that allow us to distinguish two peaks: one at 1.88 eV with an FWHM of 24 meV (indicated by a purple arrow in Figure 5a), which can potentially be assigned to the neutral exciton X^0 , and another one at 1.83 eV with an FWHM of 33 meV (indicated by a pink arrow in Figure 5a).^[10,20]

Similarly, Figure 5d plots the PL spectra of CVD and exfoliated Janus SMOSe at 300 K (dark-green spectrum) and 4 K

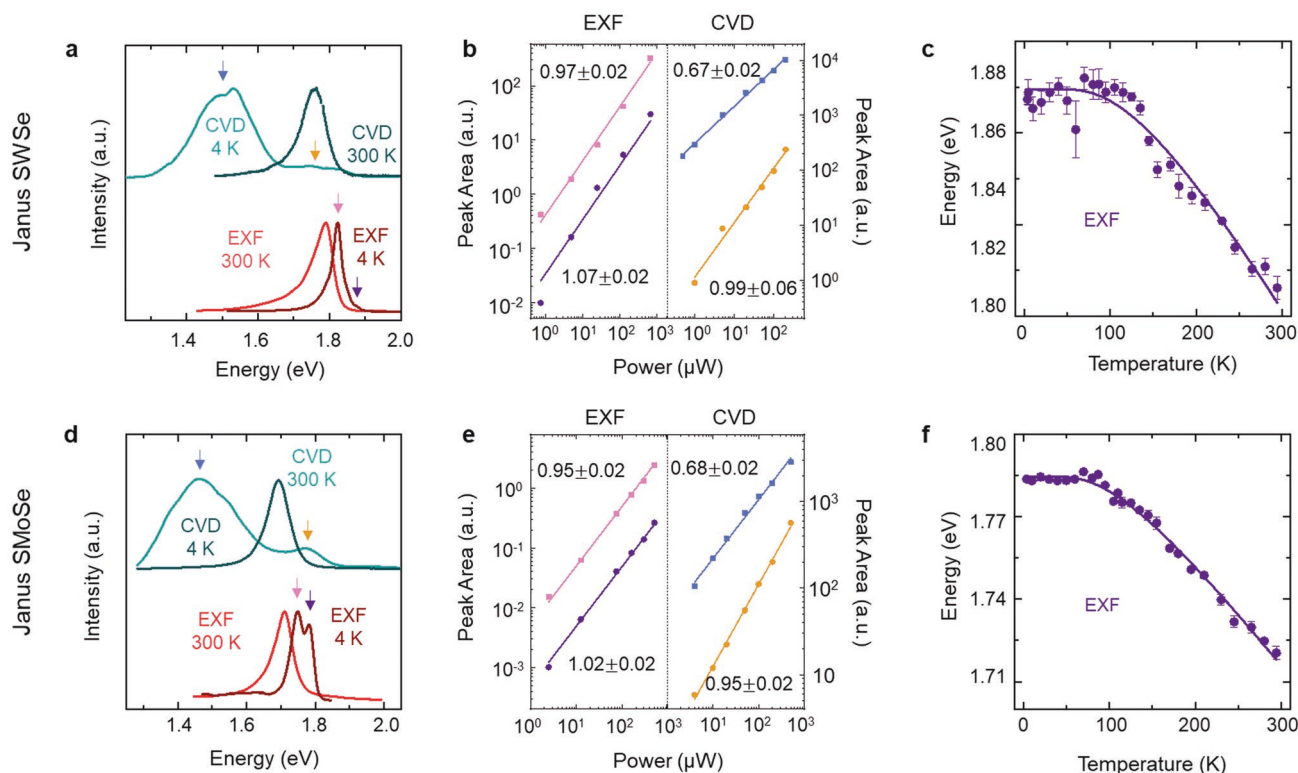


Figure 5. The first cryogenic-temperature PL characteristics of 2D Janus SWSe and SMOSe monolayers: PL measurements of Janus SWSe and SMOSe monolayers at 4 K. a) PL of CVD SWSe at 300 K (dark green spectrum) and 4 K (light green spectrum), and of exfoliated Janus at 300 K (light red spectrum) and 4 K (dark red spectrum). The arrows indicate the spectral peaks whose PL intensity is integrated to obtain the curves in (b). b) Power-dependent integrated PL intensity of the SWSe spectral peaks as a function of laser excitation power, at 4 K. The colors of the data points correspond to the colors of the arrows in (a). Left exfoliated SWSe Janus. Right: CVD-grown SWSe Janus. The solid curves are fittings of the type $I = AP^n$, where I is the integrated intensity, A is a prefactor, P is the laser excitation power, and n is the power law that describes the dependence between I and P ($n = 1$ for unbound excitons).^[33] The numbers in the panels for each curve are n . c) Energy of the higher-energy exfoliated SWSe spectral peak, indicated by the purple arrow in (a), as a function of temperature. Solid line: fitting based on semiempirical hyperbolic cotangent relationship for semiconductors.^[35] d–f) The same as (a)–(c), respectively, but for SMOSe.

(light-green spectrum). Similar to the case of SWSe Janus, the PL spectrum of a CVD Janus SMoSe monolayer dramatically changes from 300 K, which shows a PL peak at 1.69 eV and an FWHM of 72 meV, to 4 K, which shows a low energy band of FWHM of 220 meV and centered at ≈ 1.5 eV (indicated by a blue arrow in Figure 5d), with a five times smaller contribution from the peak at 1.78 eV (indicated by the orange arrow in Figure 5d). In contrast, the PL of SMoSe stemming from exfoliated monolayers at 300 K (light-red spectrum in Figure 5d) already has a narrower FWHM (59 meV) than its CVD counterpart. Upon cooling down to 4 K, the narrowing of the spectrum and lack of an X_B band allow us to distinguish two peaks: one at 1.75 eV with an FWHM of 54 meV (indicated by a pink arrow in Figure 5d) and another one at 1.79 eV (indicated by a purple arrow in Figure 5d) with an FWHM of 23 meV, which can potentially be assigned to the neutral exciton X^0 .^[10,20]

The FWHM values of the PL peaks of exfoliated Janus monolayers presented here are, to the best of our knowledge, the narrowest reported to date in the literature for Janus monolayers both at 4 and 300 K.^[4,5,10,20,31] Furthermore, the FWHM values of the highest energy peak of SWSe and SMoSe are, respectively, comparable to the FWHM of X^0 reported for exfoliated, un-encapsulated, traditional TMD monolayers at 4 K: 24 meV for SWSe versus ≈ 10 meV for WSe₂ and ≈ 15 meV for WS₂ as extracted from Figure 2b in ref. [32] and 23 meV for SMoSe versus ≈ 15 meV for MoSe₂ and ≈ 20 meV for MoS₂, as extracted from Figure 2b in ref. [32]. It is worthy to note that optical quality may further be engineered by tuning the energy of the plasma for materials of different bond energies, for instance, in Figure 5d. SMoSe at 4 K exhibits a broader PL peak than the tungsten-based counterparts for the same processing parameters due to the weaker bonds between the molybdenum and selenium atoms; as such this results in the production of greater defects' parent matrix for the same processing parameters. These values finally allow for future, reliable studies of excitonic complexes in Janus monolayers to unequivocally assign them their charging state and number of particles.^[33]

To investigate further the nature of the different peaks in the PL spectra, we perform excitation power-dependent measurements on both the CVD and exfoliated Janus monolayers at 4 K. Figure 5b shows the integrated intensities of the peaks in Figure 5a for CVD and exfoliated Janus SWSe as a function of laser excitation power, where the curve colors correspond to those of the arrows in Figure 5a. The orange curve has a slope of ≈ 1 , consistent with the peak indicated by an orange arrow in Figure 5a stemming from unbound exciton recombination.^[33] In contrast, the PL intensity of X_B , indicated by the blue arrow in Figure 5a, scales sublinearly (slope of 0.67, blue curve in Figure 5b) with the laser excitation power, confirming X_B results from defect states.^[34] The two PL peaks that can be identified in the exfoliated Janus SWSe monolayer at 4 K, indicated by pink and purple arrows in Figure 5a, both show linear dependence with excitation power, pink and purple curves in Figure 5b, demonstrating their unbound excitonic nature and the lack of X_B bands. We perform the same measurements for SMoSe and reach the same conclusions; the PL peak indicated by an orange arrow in Figure 5d for the CVD Janus SMoSe monolayer at 4 K has a linear power dependence (orange curve

in Figure 5e), while the X_B band (blue arrow in Figure 5d) of the same spectrum has a sublinear dependence (blue curve in Figure 5e). In contrast, the two identifiable PL peaks for the exfoliated-based Janus monolayer of SMoSe at 4 K (pink and purple arrows in Figure 5d) both exhibit a linear power dependence (pink and purple curves in Figure 5d).

The temperature variation of the higher-energy PL peaks, potentially X^0 , in both exfoliated SWSe (indicated by a purple arrow in Figure 5a) and exfoliated SMoSe (indicated by a purple arrow in Figure 5d) is plotted in Figure 5c,f respectively, and is fitted well with a semiempirical hyperbolic cotangent relationship based on a direct replacement of the Varshni equation^[35]

$$E_g(T) = E_g(0) - Sh\omega \left[\coth\left(\frac{h\omega}{2kT}\right) - 1 \right] \quad (1)$$

By fitting to the equation, we can extract the optical bandgap at 0 K ($E_g(0)$), the electron–phonon coupling constant (S), along with the average phonon energy in these materials ($\langle h\omega \rangle$). We obtain, for 2D exfoliated SWSe: $E_g(0) = 1.874 \pm 0.002$ eV, $S = 2.9 \pm 0.4$, and $\langle h\omega \rangle = 0.034 \pm 0.005$ eV; and for 2D exfoliated SMoSe: $E_g(0) = 1.785 \pm 0.001$ eV, $S = 2.4 \pm 0.1$, and $\langle h\omega \rangle = 0.028 \pm 0.002$ eV.

4. Conclusions

The results introduced the in situ growth process for creating most of the thermodynamically stable 2D Janus monolayers from the TMD family for the first time with an excellent excitonic quality. Integrated with the micromanipulator stage, the in situ observation of the time-resolved growth process allows for collecting the kinetics of the reaction, and the vibrational and excitonic information from micrometer-size spot regions on these Janus monolayers. The ability to monitor kinetics of the reaction and collect spectroscopic data from deterministic regions with micron accuracy makes it finally possible to convert high crystal quality 2D exfoliated monolayers into Janus structure. Together with spectroscopic monitoring tools, our approach allows us to reach growth reaction mechanisms and kinetics which, in turn, enables us to assess the quality of 2D Janus monolayers and steer the growth during the synthesis process. High excitonic and structural quality Janus monolayers enabled by the in situ growth technique are anticipated to open new quantum directions by probing a variety of predicted phenomena that have not been tested to date. Furthermore, with its in situ and deterministic nature, the technique is likely to open the experimental library of 2D Janus monolayers well-beyond TMDs by closely monitoring the Janus conversion process on 2D classical exfoliated layers without the need to develop CVD growth methods.

5. Experimental Section

Exfoliation of TMD Monolayers: Mechanical tape exfoliation of monolayers MoSe₂, WSe₂, and NbSe₂ was achieved using a poly(dimethylsiloxane) (PDMS)-assisted transfer method. Bulk crystal was initially thinned down using Scotch tape and lifted using a PDMS stamp to reduce tape residue. The PDMS/TMD stamp was then pressed

onto a plasma-cleaned Si/SiO₂ substrate with an oxide thickness of 285 nm.

Chemical Vapor Deposition: Synthesis of monolayer transition metal dichalcogenides was performed using an atmospheric-pressure chemical vapor deposition system following techniques established in the literature.^[36] A 1 in. diameter quartz tube was supported on a single-zone Lindberg Blue M furnace. For the synthesis of molybdenum diselenide, ultrahigh purity Ar was initially supplied at 200 sccm for 30 min to purge the tube of any oxygen, and the flow rate was then adjusted to 46 sccm during the growth process. About 1 mg of MoO₃ was kept in an alumina boat at the center of the tube where the temperature was set to 760 °C. Plasma-cleaned silicon substrates with an oxide thickness of 285 nm were treated with 10 μ L of perylene-3,4,9,10-tetracarboxylic acid tetrapotassium acid salt (PTAS) and supported on the boat (polished side down). The selenium source was kept at the upstream end of the tube where the temperature was about 250 °C. The furnace was ramped at the rate of 30 °C min⁻¹, and 4 sccm hydrogen was supplied as the temperature reached growth conditions. The synthesis was carried out for 5 min, after which hydrogen supply was cut off and argon flow rate was increased to 200 sccm to promote fast cooling. Synthesis of tungsten diselenide was also carried out in a similar way, except the reaction temperature was increased to 800 °C and the reaction time was increased to 16 min.

Scanning Transmission Electron Microscopy: High-resolution scanning transmission electron microscopy was performed using an aberration-corrected NION ultraSTEM 100 electron microscope. The sample was annealed at 150 °C in ultrahigh vacuum for 10 h to reduce carbon contamination during the measurement. The microscope was operated at 60 kV with a convergence angle of 34 mrad and a probe current at 25 pA s. Exfoliated Janus samples were transferred on a quantifoil holey carbon grid by a poly(methyl methacrylate) (PMMA)-assisted transfer technique reported previously in the literature.^[37] A micromanipulator was used to align the sample under the carbon grid before the transfer as shown in the Supporting Information. The grid was then fixed in this position with the aid of needles to avoid any drift during the wet transfer process. PMMA was dropped onto the sample and cured at 150 °C for 15 min followed by the etching of the SiO₂ substrate in a 30 wt% KOH solution. The PMMA thin film was then dissolved in acetone overnight followed by a deionized (DI) water rinse. Figure S12 (Supporting Information) shows the as-transferred exfoliated monolayer SWSe sample after the acetone treatment.

Atomic Force Microscopy: Atomic force microscopy (AFM) images were recorded with NT-MDT Modular AFM. Contact-mode scanning microscopy was performed on the selected area to flatten the monolayer surface and enhance contact with substrates. Height profiles were recorded simultaneously and plotted with Gwyddion.

Conversion to Janus Structure: The selective epitaxial atomic replacement method was employed with a custom-made glass chamber. Exfoliated and CVD grown monolayers and sulfur sources were placed in the center and upstream sides of the chamber, respectively. The outlet arm of the chamber was connected to a mechanical pump and capacitance manometers to create and gauge the pressures, respectively. The chamber was first pumped down to 10 mTorr for 15 min to reduce the oxygen contaminants, followed by passage of 18 sccm H₂ to maintain a pressure of 280 mTorr. The chamber was also fitted with a copper coil wrapped around the downstream arm and connected to an RF source. Plasma was ignited at 5 W and depending on the initial material the process was carried out from 8 to 20 min.

In Situ Monitoring of SEAR Process (Laser Power, Time, and Average): The geometry of the SEAR chamber was allowed for monitoring the process using a Renishaw inVia Spectrometer fitted with a 20 \times long working distance objective lens, which gave a clearance of 20 mm between the bottom of the objective to the substrate surface. The chamber was supported using a custom-made aluminum frame and could be positioned along any direction in space using XYZ micromanipulators. Before the SEAR process, the sample was aligned with the objective of the spectrometer. The measurement was carried out with a 488 nm wavelength blue laser, with 2.5 mW of power, ten seconds of exposure, and a single acquisition per measurement.

The total number of such measurements was set up based on the processing time for different materials and typically ranged from 80 to 100 measurements per process.

Low-Temperature Photoluminescence Measurements: The PL measurements at 4 K presented in Figure 5 were all done in a closed-cycle cryostat (Attodry 1000 from Attocube systems AG). Excitation and collection passed through a home-built confocal setup with the sample in reflection geometry. Continuous-wave illumination stemmed from a 2.33 eV laser (Ventus 532 from Laser Quantum Ltd.). The PL signal was sent to a 150 line grating spectrometer (Princeton Instruments Inc.). The room-temperature measurements presented in Figure 5a,d were done using the same equipment except that the insert was not inside the closed-cycle cryostat. The excitation power from the 2.33 eV laser was varied for the saturation measurements in Figure 5b,e by rotating a continuously variable neutral density filter wheel (NDC-100C-4M from Thorlabs).

The temperature variation needed for the temperature-dependent PL measurements presented in Figure 5c,f was accomplished as follows: a) the sample was in a closed-cycle cryostat at 4 K; b) the compressor of said cryostat was turned off so that the cryostat slowly and naturally warmed up from 4 K to room temperature over a week; c) the sample temperature was set by using a temperature controller (335 Temperature Controller from LakeShore) connected to a heater inside the cryostat (where the sample was mounted); d) the temperature higher than what it would be was set if the cryostat was simply left to naturally warm up. This ensured that accessibility to all temperatures from 4 to 300 K, temperature stability over the entire PL integration time, and the slow warming up over a week minimize potential material degradation. Each data point in Figure 5c,f represents an average over ten different locations, with the error bars referring to the standard error of the mean.

Computational Methods: Density functional theory (DFT) calculations were performed by using a plane-wave basis set with a kinetic energy cut-off of 450 eV and projector-augmented-wave^[38,39] potentials, as implemented in the Vienna Ab initio Simulation Package (VASP).^[40,41] For the exchange-correlation functional, local density approximations (LDA) were used. A vacuum of 20 Å along the (001) direction was introduced to construct monolayers. During structural relaxations performed within LDA, positions of the ions were relaxed until the Hellmann–Feynman forces became less than 0.001 eV Å⁻¹. Phonons were calculated using density functional perturbation theory (DFPT)^[42] as implemented in the PHONOPY.^[43] The reciprocal space integration was carried out with a Γ -centered k -mesh of $24 \times 24 \times 1$ for the conventional cell, and $12 \times 12 \times 1$ for the $2 \times 2 \times 1$ supercell used in phonon calculations.

Supporting Information

Supporting Information is available from the Wiley Online Library or from the author.

Acknowledgements

Y.Q. and M.S. contributed equally to this work. S.T. acknowledges support from DOE-SC0020653, Applied Materials Inc., NSF CMMI 1825594, NSF DMR-1955889, NSF CMMI-1933214, NSF DMR-1904716, NSF 1935994, and NSF ECCS 2052527 and DMR 2111812. A.S.B. acknowledges support from NSF DMR-1904716. The authors acknowledge the use of facilities within the Eyring Materials Center at Arizona State University and the ASU research computing center. D.M.K. acknowledges support from the Royal Society University Research Fellowship URF\R1\180593, M.S.G.F. acknowledges the EPSRC Doctoral Training Programme, and A.R.-P.M. and M.A. acknowledge the Faraday Institution FIRG001.

Conflict of Interest

The authors declare no conflict of interest.

Data Availability Statement

The data that support the findings of this study are available from the corresponding author upon reasonable request.

Keywords

2D materials, in situ synthesis, Janus materials, quantum materials

Received: August 10, 2021

Revised: November 10, 2021

Published online: December 22, 2021

- [1] J. R. Schaibley, H. Yu, G. Clark, P. Rivera, J. S. Ross, K. L. Seyler, W. Yao, X. Xu, *Nat. Rev. Mater.* **2016**, 1, 16055.
- [2] Q. H. Wang, K. Kalantar-Zadeh, A. Kis, J. N. Coleman, M. S. Strano, *Nat. Nanotechnol.* **2012**, 7, 699.
- [3] M. Yagmurcukardes, Y. Qin, S. Ozen, M. Sayyad, F. M. Peeters, S. Tongay, H. Sahin, *Appl. Phys. Rev.* **2020**, 7, 011311.
- [4] J. Zhang, S. Jia, I. Kholmanov, L. Dong, D. Er, W. Chen, H. Guo, Z. Jin, V. B. Shenoy, L. Shi, J. Lou, *ACS Nano* **2017**, 11, 8192.
- [5] A.-Y. Lu, H. Zhu, J. Xiao, C.-P. Chuu, Y. Han, M.-H. Chiu, C.-C. Cheng, C.-W. Yang, K.-H. Wei, Y. Yang, Y. Wang, D. Sokaras, D. Nordlund, P. Yang, D. A. Muller, M.-Y. Chou, X. Zhang, L.-J. Li, *Nat. Nanotechnol.* **2017**, 12, 744.
- [6] Y. C. Cheng, Z. Y. Zhu, M. Tahir, U. Schwingenschlögl, *Europhys. Lett.* **2013**, 102, 57001.
- [7] Q. Feng, N. Mao, J. Wu, H. Xu, C. Wang, J. Zhang, L. Xie, *ACS Nano* **2015**, 9, 7450.
- [8] W. Wen, Y. Zhu, X. Liu, H.-P. Hsu, Z. Fei, Y. Chen, X. Wang, M. Zhang, K.-H. Lin, F.-S. Huang, Y.-P. Wang, Y.-S. Huang, C.-H. Ho, P.-H. Tan, C. Jin, L. Xie, *Small* **2017**, 13, 1603788.
- [9] D. Hajra, R. Sailus, M. Blei, K. Yumigeta, Y. Shen, S. Tongay, *ACS Nano* **2020**, 14, 15626.
- [10] D. B. Trivedi, G. Turgut, Y. Qin, M. Y. Sayyad, D. Hajra, M. Howell, L. Liu, S. Yang, N. H. Patoary, H. Li, M. M. Petric, M. Meyer, M. Kremser, M. Barbone, G. Soavi, A. V. Stier, K. Müller, S. Yang, I. S. Esqueda, H. Zhuang, J. J. Finley, S. Tongay, *Adv. Mater.* **2020**, 32, 2006320.
- [11] R. Sant, M. Gay, A. Marty, S. Lisi, R. Harrabi, C. Vergnaud, M. T. Dau, X. Weng, J. Coraux, N. Gauthier, O. Renault, G. Renaud, M. Jamet, *npj 2D Mater. Appl.* **2020**, 4, 41.
- [12] Y.-C. Lin, C. Liu, Y. Yu, E. Zarkadoulas, M. Yoon, A. A. Puzos, L. Liang, X. Kong, Y. Gu, A. Strasser, H. M. Meyer, M. Lorenz, M. F. Chisholm, I. N. Ivanov, C. M. Rouleau, G. Duscher, K. Xiao, D. B. Geohegan, *ACS Nano* **2020**, 14, 3896.
- [13] T. Hu, F. Jia, G. Zhao, J. Wu, A. Stroppa, W. Ren, *Phys. Rev. B* **2018**, 97, 235404.
- [14] H. Xu, H. Wang, J. Zhou, Y. Guo, J. Kong, J. Li, *npj Comput. Mater.* **2021**, 7, 31.
- [15] J. Liang, W. Wang, H. Du, A. Hallal, K. Garcia, M. Chshiev, A. Fert, H. Yang, *Phys. Rev. B* **2020**, 101, 184401.
- [16] G. Plechinger, J. Mann, E. Preciado, D. Barroso, A. Nguyen, J. Eroms, C. Schüller, L. Bartels, T. Korn, *Semicond. Sci. Technol.* **2014**, 29, 064008.
- [17] M. O'Brien, N. McEvoy, D. Hanlon, T. Hallam, J. N. Coleman, G. S. Duesberg, *Sci. Rep.* **2016**, 6, 19476.
- [18] F. Li, W. Wei, P. Zhao, B. Huang, Y. Dai, *J. Phys. Chem. Lett.* **2017**, 8, 5959.
- [19] L. Ju, M. Bie, X. Tang, J. Shang, L. Kou, *ACS Appl. Mater. Interfaces* **2020**, 12, 29335.
- [20] M. M. Petric, M. Kremser, M. Barbone, Y. Qin, Y. Sayyad, Y. Shen, S. Tongay, J. J. Finley, A. R. Botello-Méndez, K. Müller, *Phys. Rev. B* **2021**, 103, 035414.
- [21] H. Sahin, S. Tongay, S. Horzum, W. Fan, J. Zhou, J. Li, J. Wu, F. M. Peeters, *Phys. Rev. B* **2013**, 87, 165409.
- [22] S. G. Drapcho, J. Kim, X. Hong, C. Jin, S. Shi, S. Tongay, J. Wu, F. Wang, *Phys. Rev. B* **2017**, 95, 165417.
- [23] A. Taghizadeh, U. Leffers, T. G. Pedersen, K. S. Thygesen, *Nat. Commun.* **2020**, 11, 3011.
- [24] J. Liu, T. W. Lo, J. Sun, C. T. Yip, C. H. Lam, D. Y. Lei, *J. Mater. Chem. C* **2017**, 5, 11239.
- [25] J. Meng, G. Wang, X. Li, X. Lu, J. Zhang, H. Yu, W. Chen, L. Du, M. Liao, J. Zhao, P. Chen, J. Zhu, X. Bai, D. Shi, G. Zhang, *Small* **2016**, 12, 3770.
- [26] X. Cui, Z. Kong, E. Gao, D. Huang, Y. Hao, H. Shen, C.-A. Di, Z. Xu, J. Zheng, D. Zhu, *Nat. Commun.* **2018**, 9, 1301.
- [27] B. Chen, Q. Yu, Q. Yang, P. Bao, W. Zhang, L. Lou, W. Zhu, G. Wang, *RSC Adv.* **2016**, 6, 50306.
- [28] F. Cadiz, S. Tricard, M. Gay, D. Lagarde, G. Wang, C. Robert, P. Renucci, B. Urbaszek, X. Marie, *Appl. Phys. Lett.* **2016**, 108, 251106.
- [29] Z. He, X. Wang, W. Xu, Y. Zhou, Y. Sheng, Y. Rong, J. M. Smith, J. H. Warner, *ACS Nano* **2016**, 10, 5847.
- [30] K. Chen, R. Ghosh, X. Meng, A. Roy, J.-S. Kim, F. He, S. C. Mason, X. Xu, J.-F. Lin, D. Akinwande, S. K. Banerjee, Y. Wang, *npj 2D Mater. Appl.* **2017**, 1, 15.
- [31] T. Zheng, Y.-C. Lin, Y. Yu, P. Valencia-Acuna, A. A. Puzos, R. Torsi, C. Liu, I. N. Ivanov, G. Duscher, D. B. Geohegan, Z. Ni, K. Xiao, H. Zhao, *Nano Lett.* **2021**, 21, 931.
- [32] F. Cadiz, E. Courtade, C. Robert, G. Wang, Y. Shen, H. Cai, T. Taniguchi, K. Watanabe, H. Carrere, D. Lagarde, M. Manca, T. Amand, P. Renucci, S. Tongay, X. Marie, B. Urbaszek, *Phys. Rev. X* **2017**, 7, 021026.
- [33] M. Barbone, A. R.-P. Montblanch, D. M. Kara, C. Palacios-Berraquero, A. R. Cadore, D. De Fazio, B. Pingault, E. Mostaani, H. Li, B. Chen, K. Watanabe, T. Taniguchi, S. Tongay, G. Wang, A. C. Ferrari, M. Atatüre, *Nat. Commun.* **2018**, 9, 3721.
- [34] S. Tongay, J. Suh, C. Ataca, W. Fan, A. Luce, J. S. Kang, J. Liu, C. Ko, R. Raghunathanan, J. Zhou, F. Ogletree, J. Li, J. C. Grossman, J. Wu, *Sci. Rep.* **2013**, 3, 2657.
- [35] K. P. O'Donnell, X. Chen, *Appl. Phys. Lett.* **1991**, 58, 2924.
- [36] X. Wang, Y. Gong, G. Shi, W. L. Chow, K. Keyshar, G. Ye, R. Vajtai, J. Lou, Z. Liu, E. Ringe, B. K. Tay, P. M. Ajayan, *ACS Nano* **2014**, 8, 5125.
- [37] Y. B. Lee, H. Jang, C. W. Ahn, *J. Nanosci. Nanotechnol.* **2016**, 16, 1810.
- [38] P. E. Blöchl, *Phys. Rev. B* **1994**, 50, 17953.
- [39] G. Kresse, D. Joubert, *Phys. Rev. B* **1999**, 59, 1758.
- [40] G. Kresse, J. Furthmüller, *Comput. Mater. Sci.* **1996**, 6, 15.
- [41] G. Kresse, J. Furthmüller, *Phys. Rev. B* **1996**, 54, 11169.
- [42] S. Baroni, S. De Gironcoli, A. Dal Corso, P. Giannozzi, *Rev. Mod. Phys.* **2001**, 73, 515.
- [43] A. Togo, I. Tanaka, *Scr. Mater.* **2015**, 108, 1.